On the Preliminary Design and Performance Prediction of Centrifugal Turbopumps – Part 2

Luca d'Agostino,[1 a] Dario Valentini,[1] Angelo Pasini,[1] Lucio Torre,[2] Giovanni Pace[1] and Angelo Cervone[3]

[1] Dipartimento di Ingegneria Civile ed Industriale, Università di Pisa, Pisa, Italy
[2] Alta S.p.A., Ospedaletto (Pisa), Italy
[3] T.U. Delft, Delft, The Netherlands

Abstract

The ideal flow model for the preliminary design and performance prediction of radial turbopumps presented in the companion paper of the present volume (d'Agostino et al., 2017) is here interfaced with the calculation of the boundary layers inside the blade channels and other major forms of flow losses, with the aim of developing an effective tool for rapid parametric optimization of the machine performance and geometry under appropriate design constraints, such as assigned values of the specific speed, flow coefficient and blade solidity. A mixed-flow turbopump, with a six-bladed impeller, a vaneless diffuser, a single-spiral volute and nondimensional performance characteristics similar to those typically used in liquid propellant rocket engine feed systems, has been designed, parametrically optimized and manufactured in accordance with the indications of the present model. The pumping and suction performance of the machine have been determined in a series of tests in the Cavitating Pump Rotordynamic Test Facility (CPRTF). Under fully-wetted flow conditions the measured pumping characteristics of the machine (hydraulic head and efficiency as functions of the flow coefficient) proved to be in excellent agreement with the model predictions, thus successfully confirming the validity of the proposed model as an effective tool for rapid and efficient design of high-performance centrifugal turbopumps.

1. Introduction

Performance, simplicity, reliability, operating range and cost-effectiveness are some of the assets that make centrifugal pumps a very popular component of an

[a] The present work has been supported by the European Space Agency under Contract No. 40001025856/10/NL/SFe. The authors would like to express their gratitude to Dr. Giorgio Saccoccia of ESA-ESTEC for his constant and friendly encouragement.

almost endless variety of liquid management systems. More specifically, high power-density turbopumps currently represents the most weight-effective solution for liquid propellant feed systems of rocket engines for primary space propulsion. These applications are in fact characterized by the joint requirements for high total and specific impulses, where large amounts of usually cryogenic propellants are to be injected at high pressures in the engine's combustion chamber. Under these conditions turbopump-fed systems are preferable, because the mass reduction allowed by the use of low-pressure tanks far outbalances the additional weight of the machine.

Typically, in modern liquid propellant rocket engine feed systems an axial inducer is also present upstream of the main pump in order to increase its suction performance, while the desired delivery pressure is mostly generated by a suitable number of mixed-flow centrifugal stages. Severe limitations are associated with the design of the high power-density, dynamically stable turbomachines capable of meeting the extremely demanding pumping, suction and reliability requirements of modern space transportation systems (Stripling and Acosta, 1962). In these applications operation under limited cavitation conditions is usually tolerated in order to minimize the weight of the propellant storage system, exposing rocket engine feed turbopumps to the onset of dangerous fluid dynamic and rotordynamic instabilities (d'Agostino, 2013a; d'Agostino, 2013b).

The design of centrifugal turbopumps determines about 80% of their final cost (Busby et al., 2008), and therefore its importance cannot be underestimated. Usually, it starts with the development a 2D flow model, which is progressively refined in a sequence of iterative trades between architectural, fluid dynamic, mechanical, structural, rotordynamic, manufacturing and assembling aspects of the pump, until the relevant requirements and specifications are met. The definition of the inducer/impeller bladings, as well as of the flowpaths in the diffuser (if any) and the volute, is typically finalized at this stage of the design process. Next, steady-state 3D fluid dynamic and structural analyses are carried out and additional details are included, as required by the specific application. Off-design, transient and unsteady flow analyses finally complete the design process.

Optimization strategies based on the Radial Basis Neural Network (RBNN) have recently been applied by many researches to the design of turbopumps (Huppertz et al., 2007; Kim et al., 2010; Choi et al., 2010; Rai and Madyavan, 2000; Kim et al., 2011). Other systematic optimization approaches commonly used in the refinement of the design of turbopumps are based on mean streamline analyses (Oh and Kim, 2011), three-dimensional inverse methods coupled with optimization algorithms (Ashihara and Goto, 2011), and steady/unsteady numerical flow simulations (Visser, Dijkers and op de Woerd, 2000). Significant efforts are currently being developed for accurately predicting and improving the performance of turbopumps with the help of complex 3D simulations and numerical optimization

methods, which are extremely demanding in terms of computational time and power (Laskshminarayana, 1985).

However, the expensive iterative nature of this approach intrinsically imposes significant limitations to its effective use for preliminary design of turbopumps. On the other hand, the availability of rational and efficient tools, capable of rapidly providing a realistic and accurate definition of both the machine geometry and performance since the early stages of its design, translates into very significant advantages for turbopump engineers and manufacturers. Up to date, however, efficient methods with these characteristics are lacking, and their development has therefore been selected as the main focus of the work illustrated in this publication.

The present activity starts from the observation that the ideal flow model illustrated in a companion paper (d'Agostino et al., 2017) proved to be quite efficient in making use of the relevant conservation equations for rationally deducing realistic geometries of mixed-flow centrifugal turbopumps specifically designed for locating the occurrence of cavitation on the initial portion of the blades, where its destabilizing effects on the flow field are less pronounced. On the other hand, the ideal flow approximation clearly prevented this model from being equally effective in the accurate prediction of the pumping performance of the machine.

In order to overcome this limitation, in the present approach the above flow model has been interfaced with the calculation of the boundary layers inside the blade channels and of other major forms of fluid dynamic losses (d'Agostino et al., 2012), with the aim of developing an effective tool for rapid parametric optimization of the machine geometry and performance under appropriate design constraints such as, for instance, assigned values of the specific speed, flow coefficient and blade solidity. The combined model has then been used, in conjunction with a standard parametric maximization algorithm, to design and optimize a mixed-flow turbopump (named VAMPIRE) with a six-bladed impeller, a vaneless diffuser, a single-spiral volute and nondimensional performances similar to those typical of space rocket applications (Pasini et al., 2011). The pumping and suction characteristics of the VAMPIRE pump have been determined in a series of steady operation tests in the Cavitating Pump Rotordynamic Test Facility (CPRTF). Finally, the measured pumping characteristics (hydraulic head and efficiency) of the machine have been compared with the theoretical predictions, with the aim of assessing and confirming the validity of the proposed model.

2. Hydraulic Losses and Efficiency

The main fluid dynamic losses to be considered for more realistic performance prediction and optimization of mixed-flow centrifugal turbopumps typically arise from flow incidence at the leading edges of the impeller blades and the volute tongue, from viscous and secondary flow effects in the impeller, and from turbu-

lent mixing in the diffuser and the volute, as schematically indicated in Figure 1.

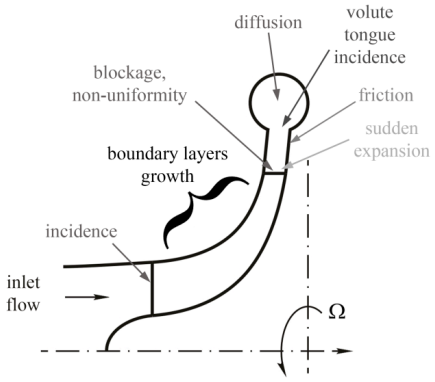

Figure 1. The main sources of losses included in the model and their locations in the machine.

Their contributions have been included in the present model and are illustrated in detail in this Section.

Notice that, in order to provide effective indications for parametric optimization of the machine, the evaluation of fluid dynamic losses must be sensitive to specific and relatively small changes of the geometry of the various components. Standard empirical loss correlations, such as those commonly used for preliminary assessment of viscous, slip flow and turbulent mixing effects in centrifugal impellers, are therefore inadequate to this purpose, and have therefore been replaced here by more detailed and realistic loss models.

2.1 Impeller

Incidence losses due to the sudden change of the flow direction at the leading edge of the inducer blades are expressed in terms of the nondimensional equivalent length $L_{eq} = D_{ch}\Delta\alpha/3$ (function of the turning angle $\Delta\alpha$, in degrees, evaluated on the mean streamline) by means of:

$$\Delta p_{tI1} = f\left(\frac{L_{eq}}{D_{ch}}\right)\frac{1}{2}\rho V_1'^2$$

where ρ is the density of the liquid, V_1' is the relative flow velocity at the mean inlet radius and the friction factor f is obtained from Moody's chart using the

Reynolds number based on the hydraulic diameter D_{ch} and the relative roughness

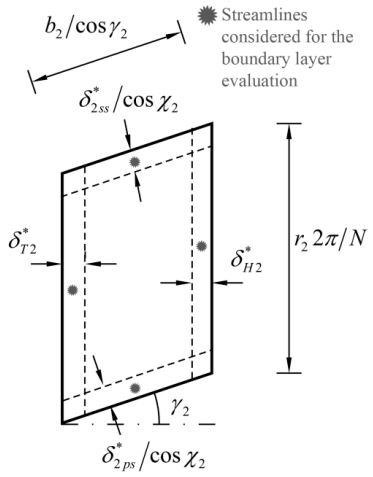

Figure 2. Schematic for the approximate evaluation of BL blockage effects at the exit section of the impeller blade channels.

of the blade channel.

Viscous effects developing on the surfaces of the blade channels generate frictional losses, flow blockage and, as a consequence of the asymmetric growth of the boundary layers on the pressure and suction sides of the blades, deviation of the flow at the impeller discharge. Moreover, the effective flow cross-section is also reduced by the blade thickness.

In order to account for the influence of these aspects on the pumping performance of the machine, the evolution of the boundary layers has been evaluated along the four streamlines passing through the mid-points of the blade channel sides at the impeller exit. The results so obtained have been considered as representative of the average viscous effects on the corresponding surfaces, as schematically illustrated in Figure 2.

Consequently, the flow blockage at the impeller exhaust has been approximated by the following expression:

$$B_{BL2} \simeq \frac{1}{A_{ch}}\left[\delta^*_{H2}\left(\frac{2\pi r_2}{N}-\frac{\delta^*_{2ss}}{\cos\chi_2}\right)+\delta^*_{T2}\left(\frac{2\pi r_2}{N}-\frac{\delta^*_{2ps}}{\cos\chi_2}\right)+\right.$$

$$+\frac{\delta^*_{2ss}\left(b_2-\delta^*_{T2}\right)}{\cos\chi_2}+\frac{\delta^*_{2ps}\left(b_2-\delta^*_{H2}\right)}{\cos\chi_2}\Bigg]$$

where δ^*_{2ss}, δ^*_{2ps} and δ^*_{H2}, δ^*_{T2} are respectively the displacement BL thicknesses on the suction and pressure sides of the blades and on the impeller hub and tip, while b_2 is the exhaust axial blade height, N is the blade number and A_{ch} is the nominal channel area. Then the flow velocity at the impeller exit, corrected for blockage effects, is:

$$\boldsymbol{u}'_{2b}=\frac{\boldsymbol{u}'_2}{\left(1-B_2\right)}$$

where $B_2=B_{B2}+B_{BL2}$ is the total blockage at the impeller exit ($r=r_2$), sum of the contributions generated by the blade thickness and the boundary layers.

The flow deviation generated by the boundary layer growth at the impeller exhaust mainly affects the azimuthal velocity and is expressed by:

$$\delta^\circ_2=\frac{1}{2}\left(\left.\frac{d\delta^*_{ss}}{dx}\right|_2\sin\lambda_{ss2}-\left.\frac{d\delta^*_{ps}}{dx}\right|_2\sin\lambda_{ps2}\right)$$

where x is the curvilinear coordinate along the streamline and λ is the angle between the rotational axis and the streamline in the meridional plane. With these corrections the relative azimuthal velocity at the impeller discharge becomes:

$$v'_{2b\delta^\circ}=-u'_{2b}\tan\left[-\tan^{-1}\left(v'_{2b}/u'_{2b}\right)+\delta^\circ_2\right]$$

Similarly, with the same approach used for the evaluation of viscous blockage effects (Figure 2), the total pressure loss at the impeller exhaust due to boundary layer friction is expressed by:

$$\Delta p_{tBL2}\simeq\frac{\theta_{H2}}{A_{ch}}\left(\frac{2\pi r_2}{N}-\frac{\theta_{2ss}}{\cos\chi_2}\right)\frac{\rho U'^2_{H2}}{2}+\frac{\theta_{T2}}{A_{ch}}\left(\frac{2\pi r_2}{N}-\frac{\theta_{2ps}}{\cos\chi_2}\right)\frac{\rho U'^2_{T2}}{2}+$$

$$+\frac{\theta_{2ss}\left(b_{I2}-\theta_{T2}\right)}{A_{ch}\cos\chi_2}\frac{\rho U'^2_{ss2}}{2}+\frac{\theta_{2ps}\left(b_{I2}-\theta_{H2}\right)}{A_{ch}\cos\chi_2}\frac{\rho U'^2_{ps2}}{2}$$

where θ_{2ss}, θ_{2ps} and θ_{H2}, θ_{T2} are the momentum boundary layer thicknesses on the suction and pressure sides of the blades and on the impeller hub and tip and U' is the streamwise velocity of the free stream in the relative frame.

The streamlines for the evaluation of the boundary layers along the impeller blade channels have been determined by numerical integration of the relevant

ordinary differential equations:

$$\frac{dr}{dx} = \frac{u'}{\sqrt{u'^2 + v'^2 + w'^2}}$$

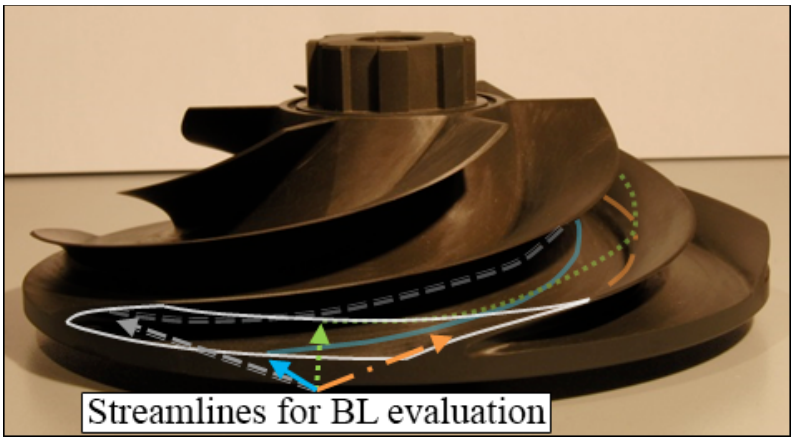

Figure 3. Relative streamlines of the inviscid flow on the impeller blade channels for turbulent BL computations.

$$\frac{d\vartheta'}{dx} = \frac{v'}{r\sqrt{u'^2 + v'^2 + w'^2}}$$

$$\frac{dz}{dx} = \frac{w'}{\sqrt{u'^2 + v'^2 + w'^2}}$$

using the relative velocity field obtained from the ideal flow model and the appropriate (final) conditions at the impeller discharge (Figure 3).

The governing equations for the laminar incompressible boundary layers on the impeller blades have then been obtained by writing the relative continuity and momentum equations:

$$\nabla \cdot \boldsymbol{u}' = 0$$

$$\boldsymbol{u}' \cdot \nabla \boldsymbol{u}' = -\frac{1}{\rho}\nabla p + \nu \nabla \cdot \left[\nabla \boldsymbol{u}' + (\nabla \boldsymbol{u}')^T \right] - 2\boldsymbol{\Omega} \times \boldsymbol{u}' + \Omega^2 \boldsymbol{r}$$

in body-fitted coordinates x and y along the streamwise and normal directions. Coriolis forces are intrinsically small in the inner layers where the relative flow velocity is low, and approximately accounted for in the outer layers by the matching with the freestream velocity, which includes the vorticity correction. Hence, with usual quasi-parallel flow approximations and neglecting Coriolis forces, obtain:

$$\frac{\partial(r_0 u_x)}{\partial x} + r_0 \frac{\partial u_y}{\partial y} = 0$$

$$u_y \frac{\partial u_x}{\partial y} + u_x \frac{\partial u_x}{\partial x} = -\frac{1}{\rho}\frac{\partial p}{\partial x} + \nu \frac{\partial^2 u_x}{\partial y^2} + \Omega^2 r \sin\lambda \cos\mu$$

$$0 \simeq -\frac{1}{\rho}\frac{\partial p}{\partial y} + \Omega^2 r_0 \cos\lambda$$

where r_0 is the radial distance from the axis, λ is the meridional angle of the boundary layer surface from the axial z-direction and μ is the angle of the boundary layer free streamline from the meridional plane.

The pressure can now be eliminated by differentiating the steady Bernoulli's equation:

$$\frac{p}{\rho} + \frac{1}{2}\left(\boldsymbol{U}' \cdot \boldsymbol{U}' - \Omega^2 \boldsymbol{r} \cdot \boldsymbol{r}\right) = \text{constant}$$

along a relative streamline:

$$-\frac{1}{\rho}\frac{\partial p}{\partial x} \simeq U\frac{dU}{dx} - \Omega^2 r \frac{dr_0}{dx} \simeq U\frac{dU}{dx} - \Omega^2 r_0 \sin\lambda\cos\mu$$

$$-\frac{1}{\rho}\frac{\partial p}{\partial y} = -\Omega^2 r \frac{dr}{dy} \simeq -\Omega^2 r_0 \cos\lambda$$

where U is the relative streamwise velocity of the freestream.

In the stated assumptions centrifugal effects in the boundary layer and in the freestream balance each other. Hence, the momentum equation in the normal direction y is identically satisfied, while in the streamwise direction x reduces to:

$$u_y \frac{\partial u_x}{\partial y} + u_x \frac{\partial u_x}{\partial x} = U\frac{dU}{dx} + \nu \frac{\partial^2 u_x}{\partial y^2}$$

(independent on Ω).

Finally, the equations for the turbulent boundary layers on the impeller blades can be obtained by standard Reynolds averaging in the form:

$$\frac{\partial\left(r_0\overline{u}_x\right)}{\partial x}+\frac{\partial\left(r_0\overline{u}_y\right)}{\partial y}=0$$

$$\overline{u}_x\frac{\partial\overline{u}_x}{\partial x}+\overline{u}_y\frac{\partial\overline{u}_x}{\partial y}=U\frac{dU}{dx}+\frac{1}{\rho}\frac{\partial\tau_t}{\partial y}$$

where bars indicate the mean flow properties, primes the turbulent fluctuations and $\tau_t=\mu\partial\overline{u}_x/\partial y-\rho\overline{u_x'u_y'}$ is the turbulent shear stress (equal to τ_w at the wall).

These equations have been solved by extending the method proposed by White (1974) to axisymmetric configurations, as required for application to mixed-flow impellers. The basic idea of White's method consists in eliminating $\overline{u}_y$ with the continuity equation and integrating the boundary layer momentum equation from the blade surface ($y=0$) to the freestream ($y=\delta$). The velocity profile is approximated by the logarithmic law of the wall:

$$u^+\simeq\frac{1}{0.4}\ln y^+ + 5.5 + w\left(y^+,\xi\right)$$

expressed in terms of the inner variables:

$$u^+=\frac{\overline{u}_x}{v^*};\quad v^+=\frac{\overline{u}_y}{v^*};\quad y^+=\frac{yv^*}{\nu}$$

with frictional velocity $v^*=\sqrt{\tau_w/\rho}$ and an outer wake $w\left(x,y^+\right)=0.6y^+\xi(x)$, linear in y^+ and in the pressure-gradient correlation parameter (Mellor, 1966):

$$\xi(x)=\frac{\mu U}{\tau_w v^*}\frac{dU}{dx}$$

Upon introduction of the nondimensional streamwise coordinate $x_*=x/2r_2$ and freestream velocity $U_*=U/\Omega r_2$, the following ordinary differential equation for the skin friction parameter $\lambda=U^+$ has been obtained (Valentini, 2011; d'Agostino et al. 2012; Valentini, 2015):

$$\frac{d\lambda}{dx_*}=\frac{U_*\mathrm{Re}_D-\left[\lambda^2\delta^+-G(\lambda,\xi)\right]\lambda\dfrac{d\ln U_*}{dx_*}+\dfrac{\lambda^4H(\lambda,\xi)}{\mathrm{Re}_D}\dfrac{d^2}{dx_*^2}\left(U_*^{-1}\right)-K(\lambda,\xi)\lambda\dfrac{d\ln r_0}{dx_*}}{G(\lambda,\xi)-\dfrac{3\lambda^3H(\lambda,\xi)}{\mathrm{Re}_D}\dfrac{d}{dx_*}\left(U_*^{-1}\right)}$$

Here $\mathrm{Re}_D=2\Omega r_2^2/\nu$ is the Reynolds number based on the impeller tip speed Ωr_2 and diameter $2r_2$,

$$G(\lambda,\xi)=\int_0^{\delta^+} u^{+2}\,dy^+$$

and:

$$H(\lambda,\xi)=\int_0^{\delta^+}\left(u^+\frac{\partial u^+}{\partial \xi}-\frac{\partial u^+}{\partial y^+}\int_0^{y^+}\frac{\partial u^+}{\partial \xi}dy^+\right)dy^+$$

have the same expressions as in White (1974), while:

$$K(\lambda,\xi)=\int_0^{\delta^+}\left(\frac{\partial u^+}{\partial y^+}\int_0^{y^+}u^+\,dy^+\right)dy^+$$

is an additional function to be included when $dr_0/dx\neq 0$.

The above ordinary differential equation for λ has been numerically integrated along the four relative streamlines passing through the midpoints of the blade channel sides at the impeller exit with the IC $\delta^+(0)\simeq 10$ imposed by the lower limit of validity of the law of the wall (merging with the laminar sublayer), which in turn determines the initial value of $\lambda(0)=\frac{1}{0.4}\ln 10+5.5+6\xi$.

Finally, at any location x_* the boundary layer nominal, displacement and momentum thicknesses have been computed as:

$$\delta=2r_2\frac{\delta^+\lambda}{U_*\mathrm{Re}_D};\qquad \delta^*=2r_2\frac{\delta^{*+}\lambda}{U_*\mathrm{Re}_D}\qquad\text{and}\qquad \theta=2r_2\frac{\theta^+\lambda}{U_*\mathrm{Re}_D}$$

Their evolution along the blade channels of the VAMPIRE pump operating at nominal conditions is illustrated in Figure 4. The results are similar for δ, δ^* and θ, which in turbulent boundary layers are nearly proportional to each other. Specifically, the development of the boundary layer is predicted to proceed rather regularly on the suction side of the blades and, even if not relevant to the present case of unshrouded impeller as indicated later, also on the casing surface at the blade tip radius. On the other hand, the evolution of δ, δ^* and θ is slightly more irregular on the pressure side of the blades and on the hub surface where, however, flow turning effects tend to oppose the separation of the flow. The regular growth of the boundary layer is indicative of a favorable pressure distribution and is especcialy significant on the suction side of the blades, where the flow is generally more susceptible to separation. As a whole, the results of Figure 4 fully confirm the validity of the proposed method for the definition of hydrodynamically efficient impeller geometries.

By supporting the blades on both sides, impeller shrouds can be quite useful to reduce bending stresses and flutter instabilities. But they also add to the manufacturing complexity and weight of impellers, thus reducing their critical speeds.

Besides, the narrow recirculating leakage flow between their outer surface and the machine casing increases ventilation losses and generates spurious and uncertain rotordynamic effects. For these reasons, whenever possible unshrouded impellers are typically favored in space applications (Droege, Williams and Garcia, 2000). In these impellers the boundary layers developing on the impeller casing are continuously wiped out by passing blades. Therefore, an approximate but practical way to

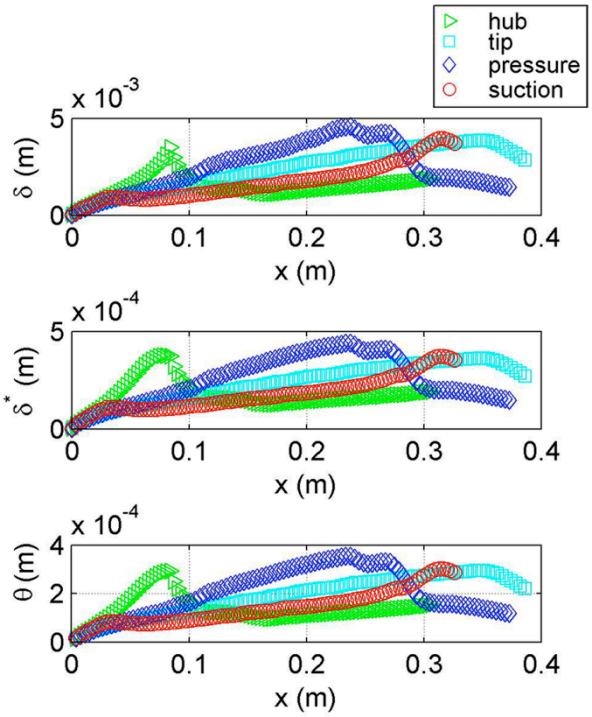

Figure 4. Streamwise evolution of the boundary layer thicknesses along the blade channels.

account for the absence of the shroud in the present model consists in simply not considering the boundary layers on the inner surface of the impeller casing.

The above approach allows for the quantitative evaluation of viscous effects (blockage, deviation and losses) taking place in the flow through centrifugal impel-

lers as functions of their geometry and operating conditions. Perfect mixing is assumed to occur at rotor discharge at the inlet cross-section of the diffuser. The resulting total pressure losses have then been be evaluated as the mass averaged integral difference between the dynamic pressures of the mean flowfield at the diffuser inlet and the nonuniform velocity distribution at the impeller discharge station, that is:

$$\Delta p_{tM2}(z) = \frac{N}{4\pi}\rho\int_0^{2\pi/N}\left(\tilde{v}_2^2 - v_S^2\right)d\vartheta'$$

where $\tilde{v}_2$ is the local azimuthal component of the vorticity correction and v_s is the azimuthal slip velocity.

2.2 Diffuser

Friction on the side walls and the sudden increase of the flow passage area at the exit of the impeller are the main sources of fluid dynamic losses in vaneless diffusers. Frictional losses can be evaluated along the nominal streamlines (consisting in log-spirals with constant angle φ from the radial direction) by means of the expression:

$$\Delta p_{tF3} = \frac{1}{2}\rho\left(u_3^2 + v_3^2\right)f_D\frac{r_3\left(r_3 - r_2\right)}{2b_D r_2\cos\varphi}$$

where b_D is the width of the diffuser and the friction factor f_D depends on the flow Reynolds number based on the hydraulic diameter $D_{Hdiff} = 2b_D$. Finally, diffusion losses due to the sudden variation of the flow passage area from the impeller discharge to the diffuser can be estimated using the following expression:

$$\Delta p_{tD2} = \frac{1}{2}\rho\left(\overline{\boldsymbol{u}}_{b2}^2 - \boldsymbol{u}_2^2\right) = \frac{1}{2}\rho\left(\overline{u}_{b2}^2 - \overline{u}_2^2\frac{b_{I2}^2}{b_D^2}\right)$$

where $\overline{u}_{b2}$ and $\overline{u}_2$ are the average values of the radial velocity at the impeller exit with and without corrections for blockage effects.

2.3 Volute

The flow losses occurring in the volute typically include radial diffusion losses at the volute entrance, incidence losses at the tongue, frictional losses on the walls, azimuthal diffusion losses in the volute and mixing losses in the exhaust duct. The volute flowfield is relatively complex, being intrinsically 3D, unsteady, and, in most cases, turbulent. Accurate prediction of the resulting losses would in principle call for the simultaneous simulation of the entire flow through the turbopump,

quite an ambitious task, computationally very expensive and time-consuming. As anticipated in the first part of this publication (d'Agostino et al., 2017), such simulations are indeed capable of evaluating the flow properties in the volute with spatial resolution dependent on the size of the computational grid (Van den Braembussche, 2006), but do not provide any direct indication for the selection of the machine geometry, which must be assigned as a known input to the computations.

On the other hand, the present model is intended as a rapid and effective tool for simultaneous and accurate definition of the geometry of the machine and prediction of its fluid dynamic performance, as required in the preliminary phase of the design. For most efficient definition of the model it is worth noting that total pressure losses in the volutes of radial turbopumps are usually dominant, especially at off-design conditions, with respect to the contributions from other components. This is because the separated/swirling nature of the flow in the volute promotes large-scale turbulent mixing and because the geometry of the volute can only be optimally adapted to the impeller for one single value of the flow coefficient. Based on these considerations, only incidence losses at the tongue and mixing losses in the volute have been taken into account in the present model. Available evidence demonstrates that this approximation is capable of providing accurate predictions of the magnitude and trends of flow losses occurring in the volute of the test turbopump, thus supporting the conclusion that it can be safely applied to similar machines designed in accordance with the indications of the present model.

The total pressure loss due to the flow incidence at the tongue of the volute has been computed as:

$$\Delta p_{tLVi} \simeq \xi_{tLVi} \frac{1}{2} \rho \left\{ \boldsymbol{u}_3^2 - \left[\left| \boldsymbol{u}_3 \right| \cos\left(\varphi_3 - \varphi_T \right) \right]^2 \right\}$$

corresponding to the dissipation of a constant portion ξ_{tLVi} (here equal to 0.9) of the kinetic energy of the approach velocity component normal to the orientation φ_T of the tongue w.r.t. the azimuthal direction ($\varphi_T = \varphi_{3des}$ at design conditions).

For simplicity, mixing losses in the volute have been included only when the incoming flow velocity is faster than at the exit cross-section and correspond to losing a constant portion ξ_{tLVd} (here equal to 0.9) of the associated dynamic pressure change:

$$\Delta p_{tLVd} = \xi_{tLVd} \frac{1}{2} \rho \left(\boldsymbol{u}_3^2 - \boldsymbol{u}_4^2 \right)$$

Finally, frictional losses along the walls of the volute have been neglected because of their relatively small magnitude.

2.4 Overall Performance

With the above results, the pumping performance of the machine becomes:

$$\Psi = \frac{\Delta p_t}{\rho \Omega^2 r_2^2} = \frac{\Delta p_{tE2} - \Delta p_{tLOSS}}{\rho \Omega^2 r_2^2}$$

where the total pressure increase computed from Euler equation includes the effects of flow blockage and deviation generated by the BLs developing along the blade channels:

$$\Delta p_{tE2} = \rho \Omega r_2 \overline{v}_{2b\delta^\circ}$$

and the total pressure loss comprises all of the sources of dissipation considered above:

$$\Delta p_{tLOSS} = \Delta p_{t1} + \Delta p_{tBL2} + \Delta p_{tM2} + \Delta p_{tD2} + \Delta p_{tF3} + \Delta p_{tLVi} + \Delta p_{tLVd}$$

Finally, the hydraulic efficiency of the machine has been evaluated by means of the expression:

$$\eta_h = \frac{Q \Delta p_t}{\Omega \tau}$$

where Q is the volumetric flow rate, Δp_t is the total pressure increase, Ω is the rotational speed and τ is the torque applied to the pump shaft.

3. Experimental Apparatus

The Test Facility. The experimental activity reported in the present paper has been carried out in the Cavitating Pump Rotordynamic Test Facility (CPRTF, Figure 5).

This facility is specifically designed for characterizing the performance of cavitating and non-cavitating turbopumps in a wide variety of alternative configurations (axial, radial or mixed flow, with or without an inducer (Cervone et al., 2012; Pace et al., 2012; Rapposelli, Cervone and d'Agostino, 2002). It operates in water at temperatures from room conditions up to 90 °C and is intended as a flexible apparatus readily adaptable to conduct experimental investigations under hydrodynamic, Reynolds and thermal cavitation similarity conditions on virtually any kind of fluid dynamic phenomena relevant to high performance turbopumps. The test section can be equipped with a rotating dynamometer, for the measurement of the forces and moments acting on the impeller, and with a mechanism designed for adjusting and rotating the eccentricity of the impeller axis in the range 0÷2 mm and ±3000 rpm. The inlet section and mounting elements of the tur-

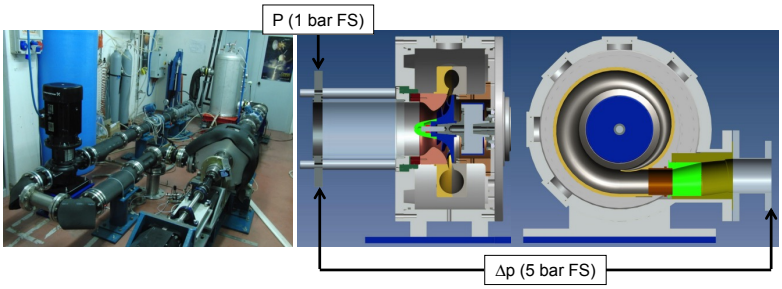

Figure 5. The Cavitating Pump Rotodynamic Test Facility (left) and cut-out of the test section showing the pump assembly and the locations of the pressure transducer (right).

bopump in the housing can be easily replaced in order to allow for testing inducers and machines with different diameters and geometries.

In present experiments the CPRTF has been equipped with the rotating dynamometer in order to eliminate the uncertainties related to friction in the seals and bearings of the shaft in the measurement of the torque applied to the pump impeller. The dynamometer is realized in one solid piece of AISI 630 H1025 phase

Figure 6. The six-bladed centrifugal impeller of the VAMPIRE turbopump.

hardening steel and consists of two flanges connected by four square pillars acting as flexing elements in a classical squirrel-cage configuration. The deformation of the pillars is measured by 40 semiconductor strain gauges arranged in 10 full Wheatstone bridges, which provide redundant measurements of the instantaneous forces and moments acting on the impeller along the axial and lateral directions.

Each bridge is temperature self-compensated, with separate bipolar excitation and read-out for better reduction of cross-talking. The inlet pressure and the pressure rise, necessary for the characterization of the pump performance, have been measured by means of an absolute pressure transducer (Druck, model PMP 1400, 0÷1.5 bar, 0.25% precision) installed about two impeller diameter upstream of the inlet cross-section and a differential pressure transducer (Druck, model PMP 5073, range 0-5 bard, 0.1% precision) installed between the inlet and the outlet sections of the test pump (with the low pressure tap at the same location as the absolute pressure tap and the high pressure tap more than one impeller diameter down-

Table 1. Main operational parameters and geometrical characteristics of the VAMPIRE turbopump.

Parameter	Units	Symbol	Value
Design flow coefficient	–	Φ	0.092
Number of blades	–	N	6.00
Outlet radius	mm	r_2	105.0
Inlet Tip radius	mm	r_{t1}	57.2
Inlet hub radius	mm	r_{h1}	31.8
Axial length (fully-developed blade)	mm	z_{h2}	46.4
Inlet tip blade angle	deg	γ_{t1}	56.60
Inlet backsweep angle	deg	χ_1	0.00
Diffuser outlet radius	mm	r_3	126.0
Rotational Speed	rpm	Ω	1500
Design volumetric flowrate	l/s	V_D	16.8
Tip solidity	–	σ_T	2.26
Incidence tip angle @ design	deg	α	17.40
Outlet tip blade mean angle	deg	γ_{t2}	67.78
Outlet tip backsweep angle	deg	χ_2	66.00
Exit blade height	mm	b_2	10.5
Exit cross-section volute radius	mm	R_4	38.2
Volute maximum radial dimension	mm	r_{V4}	201.5

stream of the exit cross-section of the volute).

The desired values of the blade tip clearance have been obtained by adjusting the inner diameter of the interchangeable casing of the impeller (see Figure 5). This feature is particularly useful when conducting rotordynamic tests in order to tailor the clearance as necessary for accommodating the imposed eccentricity of the rotor and avoiding rotor/stator contact.

Two electromagnetic flowmeters (mod. 8732E by Fisher-Rosemount, range 0-100 l/s, 0.5% precision), mounted on the suction and discharge lines, measure the pump's inlet/outlet flow rates and a thermocouple monitors the temperature of the working fluid with ±0.5 K precision.

A custom-made Silent Throttle Valve, designed for NASA by Innerspace Corp., Covina, California (USA), has been used for adjusting the pump load.

The Test Pump. The pump, named VAMPIRE, used in present experiments has been designed by means of the present model and parametrically optimized as documented in d'Agostino et al., 2012. It has been manufactured in 7075-T6 aluminum alloy, and comprises a six-bladed unshrouded impeller (see Figure 6), a vaneless diffuser and a single-spiral volute. Its main operational parameters and geometrical characteristics are summarized in Table 1.

4. Results and Discussion

A series of tests has been conducted on the VAMPIRE pump with the aim of experimentally validating the proposed model for preliminary design and noncavitating performance prediction of centrifugal pumps.

The model has been generalized in order to account for the results of a parallel test campaign aimed at investigating the influence of thermal cavitation effects on the rotordynamic whirl forces on the VAMPIRE pump with different values of the tip clearance (Pace et al., 2014, Valentini et al., 2016; Pace et al., 2016). The presence of a tip clearance in unshrouded impellers significantly increases the complexity of the flow structure. Since the detailed treatment of this aspect is too demanding in terms of additional complexity and/or computational cost of the model, a simplified approach has been adopted to approximately describe its influence on the turbopump performance.

Tip clearance changes have long been known to affect both the head and flow coefficients of the machine, as recently confirmed by some of the authors in the case of inducers (Torre et al., 2011). Specifically, the presence of blade tip clearance in unshrouded rotors involves three major effects since it:

- affects the secondary flow in the blade channels;

- induces the occurrence of tip leakage flows as a consequence of the pressure difference on the two sides of the blades;
- modifies the intermittent "scraping" caused by the blade passage on the boundary layers developing on the inner surface of the impeller casing (Koshide and Nielson, 1973).

With reference to Figure 7, the operating point of the test pump is defined by the intersection between its head characteristic and the load curve of the facility, which can be considered constant for given setting of the silent throttle valve and approx-

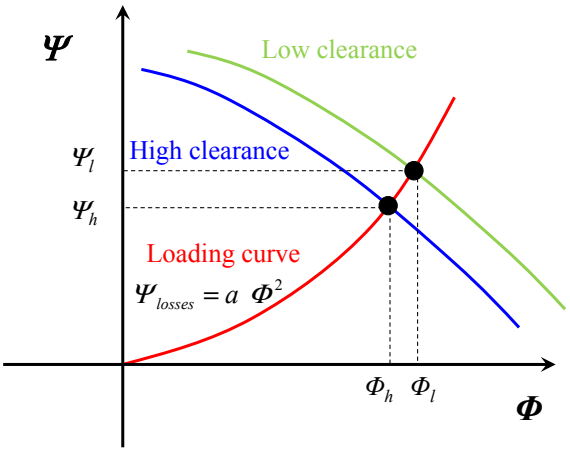

Figure 7. Noncavitating operating points (solid circles) of a turbopump respectively operating with higher (subscript *h*) and lower (subscript *l*) impeller blade tip clearances at constant settings of the test facility.

imately quadratic in the flow rate at Reynolds numbers higher than 10^6 based on the impeller tip diameter and speed. Then, all other operating conditions being the same, the relation between the head and flow coefficients of the machine for two values (subscripts *l* for lower and *h* for higher) of the blade tip clearance becomes:

$$\Phi_l = \Phi_h \sqrt{\frac{\Psi_l}{\Psi_h}}$$

This equation allows for scaling the noncavitating performance of the machine for different tip clearances once the associated head change is known. To this pur-

pose it is worth noting that, as reported in the literature (Torre et al., 2011; Koshide and Nielson, 1973; Brennen, 1994), the noncavitating head coefficient is approximately linear in the relative tip clearance ($c_{\%}$), defined as the ratio between the tip clearance (c) and the average height of the impeller blades (b_a).

With reference to Figure 8 (where the head coefficient has been nondimensionalized with its nominal design value Φ_0), the interpolating straight line for the VAMPIRE pump has been evaluated from the experimental results for two different tip clearances (squares). For any given value of the relative clearance, the corrected head coefficient is then obtained from this correlation and the corre-

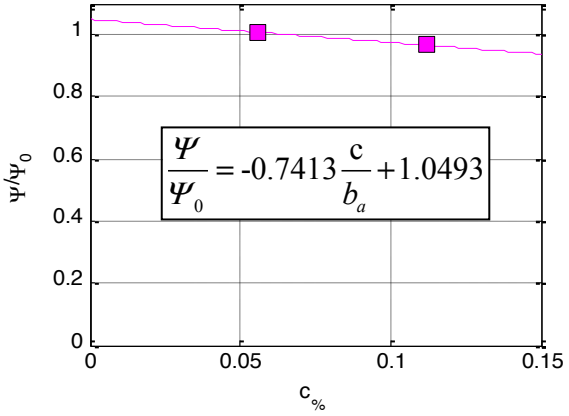

Figure 8. Normalized nondimensional head of the VAMPIRE turbopump as a function of the relative tip clearance. The linear correlation of the diagram (solid line) has been obtained from two experiments at different blade tip clearances (solid squares).

sponding flow coefficient from the above equation. In turn, these coefficients have been used to modify the pumping characteristics predicted by the model in order to account for the actual value of the blade tip clearance.

The relative tip clearances of the reference turbopump configurations used for the definition of the above correction procedure are $c_{\%}$ = 5.6% and 11.2%, corresponding to 1 and 2 mm blade tip clearances, respectively. Each experimental point has been obtained by averaging the readings of the differential pressure and flow rate acquired over 2 seconds at 5,000 sps (samples per second). In order to attain fully developed turbulent flow conditions, rotational speed of the pump and

the water temperature have been kept respectively constant at 1500 ±3 rpm and 19.5 ±1 °C, corresponding to a Reynolds number $\mathrm{Re} = 2\Omega r_2^2 / \nu = 5.01 \cdot 10^6$.

In order to validate the above procedure for tip clearance correction, two different series of tests have been conducted, where the pumping performance of the VAMPIRE pump has been measured for two different clearances equal to 1 mm ($c_{\%}$ = 5.6%) and 0.16 mm ($c_{\%}$ = 0.9%). Figure 9 shows the comparison of the experimental pumping performance (squares and upward-pointing triangles) with the corrected predictions of the analytical model (circles and stars).

Figure 9 also shows the hydraulic efficiency characteristics for the same two configurations of the pump. It is worth recalling that in the experimental evaluation

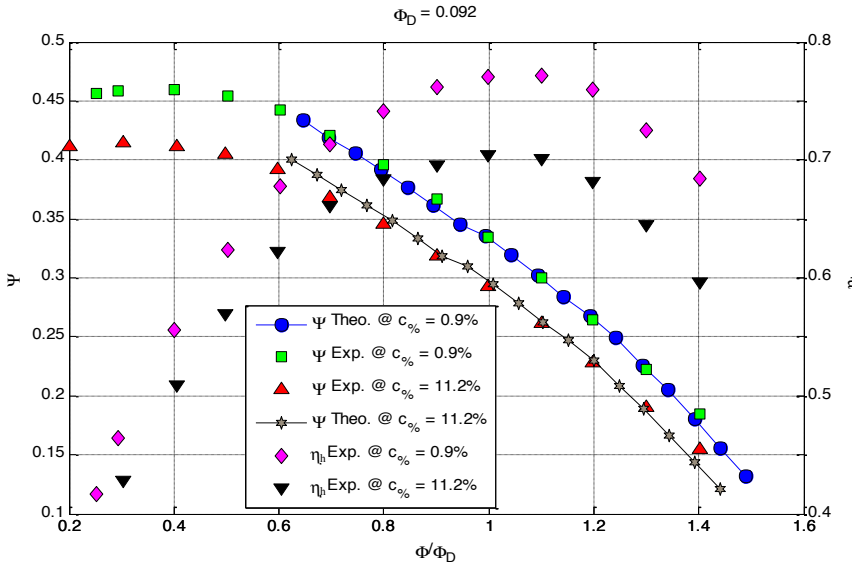

Figure 9. Normalized Comparison between the experimental and predicted (theoretical) noncavitating performance of the VAMPIRE pump operating at Ω = 1500 rpm and $\mathrm{Re} = 5.01 \cdot 10^6$ for two different values of the blade tip clearance (left scale). The figure also shows the corresponding hydraulic efficiencies (right scale).

of the hydraulic efficiency η_h the shaft power has been obtained by means of the rotating dynamometer and is therefore not affected by the uncertain influence of frictional torque in the bearings and seals.

Due to numerical limitations of the boundary-layer solver under severe flow separation on the suction/pressure sides of the impeller blades (see White, 1974), the

predictions of the model are restricted to flow coefficients in the range from 65% to 160% of the design value. Anyway, the accessible operational range of the model covers with wide margins the conditions typically encountered by liquid propellant feed turbopumps in space propulsion applications.

The relative deviations of the measured head coefficients from the theoretical results are illustrated in Figure 10 for two values of the relative blade tip clearance. The shaded area indicates the ±5% bandwidth above and below the observed performance. In the same figure the dashed and dotted lines show for each clearance setting the mean deviation between the experimental and the theoretical results. In both cases the calculated pumping performance at design conditions is quite accu-

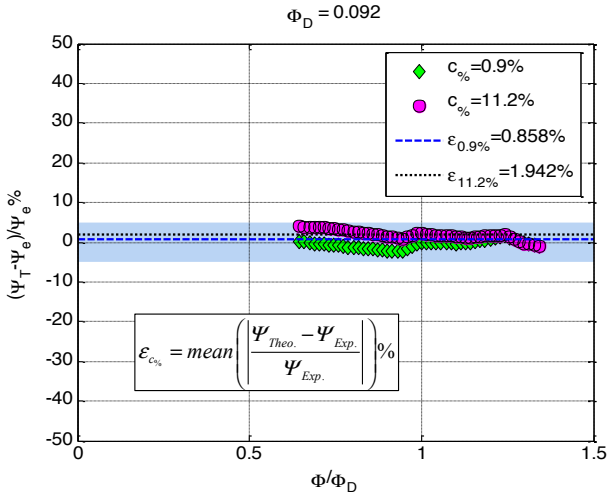

Figure 10. Relative deviation between the predicted and experimental head performance of the VAMPIRE pump for two values of the relative blade tip clearance.

rate and, in particular, in the low clearance case it is less than 0.5% off the measured value. As a whole, the results of the present investigation clearly indicate that the calculated performance closely matches the experimental measurements and successfully confirm the predictive capability of the proposed model.

5. Conclusions

The noncavitating tests conducted on the VAMPIRE turbopump, designed and parametrically optimized by means of the reduced-order model recently developed

by some of the authors and extended in the present work with the inclusion of the major sources of fluid dynamic losses, successfully confirmed that the proposed model is indeed capable of efficiently defining the geometry of mixed-flow centrifugal turbopumps and accurately predicting their non-cavitating performance.

By expressing the performance of these machines in terms of a relatively small number of controlling parameters, the proposed model is especially suited for rapid and efficient optimization. This feature has been fully and successfully exploited in the design of the VAMPIRE pump to given requirements and specifications.

For lack of space, the illustration of the optimization procedure used for the design of the test pump has been postponed to a later publication, but the quality of its results is well documented here by the very close match between the predicted and measured values of the hydraulic performance (head and efficiency) of the VAMPIRE pump. To this effect, special attention has been paid to obtaining an accurate measurement of the torque actually applied to the impeller by making use the CPRTF rotating dynamometer, thus eliminating the uncertain and spurious influence of seal and bearing torques.

The tests conducted on the VAMPIRE pump are also in excellent agreement with the semi-heuristic approach used to account for the influence on the machine performance of the impeller blade tip clearance, which is not explicitly incorporated in the model.

As a whole, the results of present experiments successfully confirm the validity of the proposed model as a very effective tool for rapid and efficient preliminary definition of the geometry and hydraulic performance of mixed-flow centrifugal turbopumps, as required in the conceptual, feasibility and initial stages of their development and design.

6. Bibliography

Adler, D., and Krimerman, Y. (1978). *The Complete 3-Dimensional Calculation of the Compressible Flow Field in Turbo Impellers*. In J. Mech. Eng.ing Sci., Vol. 20, p. 149.

Ashihara, K., and Goto, A. (2011). *Turbomachinery Blade Design using 3-D Inverse Design Method, CFD and Optimization Algorithm*. In ASME Turbo Expo, 2001.

Brennen, C. E., (1994). *Hydrodynamics of Pumps*, Oxford University Press.

Busby, J., Batton, W., Furst, R., and Ashvin, H. (2008). *High Suction Specific Speed LOX Pump: Design, Analysis and Testing*. In 44th AIAA/ASME/SAE/ASEE Joint Propulsion Conference & Exhibit, Hartford, (CT), USA.

Cervone, A., Pace, G., Torre. L., Pasini, A., and d'Agostino, L. (2012). *Effects of the Leading Edge Shape on the Performance of an Axial Three Bladed Inducer*. In 14th International Symposium on Transport Phenomena and Dynamics of Rotating Machinery, Honolulu, Hawaii, USA.

Choi, K. J., Kim, J. H., and Kim, K. Y. (2010). *Design Optimization of Circumferential Casing Grooves for a Transonic Axial Compressor to Enhance Stall Margin*. In ASME Turbo Expo 2010.

d'Agostino, L., Pasini, A., Valentini, D., Pace, G., Torre, L., Cervone, A. (2012). *A Reduced Order Model for Optimal Centrifugal Pump Design*. In: 14th Int. Symp. on Transport Phenomena and Dynamics of Rotating Machinery, ISROMAC-14, February 27th – March 2, Honolulu, HI, USA.

d'Agostino, L. (2013a). *Turbomachinery Developments and Cavitation*. In: STO-AVT-LS-206, Paper NBR 12-1, VKI Lecture Series on Fluid Dynamics Associated to Launcher Developments, von Karman Institute of Fluid Dynamics, Rhode-Saint-Genèse, Belgium, April 15-17.

d'Agostino, L. (2013b). *On the Hydrodynamics of Rocket Propellant Engine Inducers and Turbopumps*. In: 6th Intern. Conf. on Pumps and Fans with Compressors and Wind Turbines (IPCF 2013), Sep. 19-22, Beijing, China.

d'Agostino, L., Valentini, D., Pasini, A., Torre, L., and Pace, G. (2017). *On the Preliminary Design and Performance Prediction of Centrifugal Turbopumps - Part 1*. In this volume, CISM Courses and Lectures No. 1408, Int. Centre for Mechanical Sciences. d'Agostino L. and Salvetti M.V. Editors. Vien and New York: Springer.

Droege, A. R., Williams, R. W., and Garcia, R. (2000). *Unshrouded Impeller Technology Development Status*. NASA Technical Reports Server.

Huppertz, A., Flassig, P. M., Flassig, R. J., and Swoboda, M. (2007). *Knowledge-Based 2D Blade Design Using Multi-Objective Aerodynamic Optimization and a Neural Network*. In ASME Turbo Expo.

Kim, J. H., Choi, K. J., and Kim, K. Y. (2010). *Surrogate Modeling for Optimization of a Centrifugal Compressor Impeller*. In International Journal of Fluid Machinery and Systems, Vol. 3, No. 1, pp. 29-38.

Kim, J.-H., Jin, C.-H., and Kim, K.-Y. (2011). "Performance Improvement of a Mixed-Flow Pump by Optimization Techniques," in ASME-JSME-KSME Joint Fluids Engineering Conference, Hamamatsu, Japan.

Koshide, R. K., and Nielson, C. E.. (1973). *Study of Blade Clearance Effects on Centrifugal Pumps*. NASA CR-120815 R-8806.

Laskshminarayana, B. (1985). *Fluid Dynamics and Heat Transfer of Turbomachinery*. New York: John Wiley and Sons Inc.

Mellor, G.L. (1966). *The Effects of Pressure Gradients on Turbulent Flow near a Smooth Wall*, Journal of Fluid Mechanics, Vol. 24, Nº2, pp. 255-274.

Oh, H. W., and Kim, K. Y. (2011). *Conceptual Design Optimization of Mixed-Flow Pump Impellers Using Mean Streamline Analysis*. In Proceedings of the Institution of Mechanical Engineers, Part A: Journal of Power and Energy, Vol. 215, No. 1, pp. 133-138.

Pace, G., Pasini, A., Torre, L., Valentini, D. and d'Agostino, L. (2012). *The Cavitating Pump Rotordynamic Test Facility at ALTA S.p.A.: Upgraded Capabilities of a Unique Test Rig*. In Space Propulsion Conference, Bordeaux, France, 2012.

Pace, G., Valentini, D., Torre, L., Pasini, A., and d'Agostino L. (2014). *Experimental Characterization of Rotordynamic Forces Acting on Space Turbopumps*. In: Space Propulsion 2014, May 19-22, Cologne, Germany.

Pace G., Valentini D., Pasini A., Torre L., Hadavandi R., d'Agostino L. (2016). *Inducer and Centrifugal Pump Contributions to the Rotordynamic Fluid Forces Acting on a Space Turbopump*. In: ISROMAC 2016, International Symposium on Transport Phenomena and Dynamics of Rotating Machinery, Honolulu, Hawaii, USA, April 10-15.

Pasini, A., Torre, L., Cervone, A., d'Agostino, L. (2011). *Characterization of the Rotordynamic Forces on Tapered Axial Inducers by Means of a Rotating Dynamometer and High-Speed Movies*. In WIMRC 3rd International Cavitation Forum 2011, University of Warwick, UK, 4th-6th July 2011.

Rai, M. M., and Madyavan, N. K. (2000). *Aerodynamic Design Using Neural Networks*. AIAA Journal, Vol. 38, No. 1, pp. 173-182.

Rapposelli, E., Cervone, A., and d'Agostino, L. (2002). *A New Cavitating Pump Rotordynamic Test Facility*. In AIAA Joint Propulsion Conference and Exhibit, Indianapolis, USA.

Stripling, L., and Acosta, A. (1962). *Cavitation in Turbopumps – Part 1*. In ASME Journal of Basic Engineering, vol. 84, pp. 326-338, September.

Torre, L., Pasini, A., Cervone, A., Pace, G., Miloro, P., and d'Agostino, L. (2011). *Effect of Tip Clearance of the Perfomance of a Three-Bladed Axial Inducer*. In AIAA Journal of Propulsion and Power, Vol. 27, No. 4, Jul-Aug, pp. 890-898,

Valentini, D. (2011). *Sviluppo di un Modello per la Progettazione di Turbopompe Centrifughe*, M.S. Thesis, Università di Pisa, Pisa, Italy, October 10, 2011.

Valentini, D. (2015). *Modelling and Testing of Chemical Propulsion Rocket Subsystems*. Ph.D. Thesis, Università di Pisa, Pisa, Italy, December 14, 2015.

Valentini, D., Pace, G., Pasini, A., Torre, L., Hadavandi, R., and d'Agostino, L. (2016). *Fluid-Induced Rotordynamic Forces on a Whirling Centrifugal Pump*. In: ISROMAC 2016, International Symposium on Transport Phenomena and Dynamics of Rotating Machinery, Honolulu, Hawaii, USA, April 10-15

Van den Braembussche, R. A. (2006). *Flow and Loss Mechanism in Volutes of Centrifugal Pumps*. In: Design and Analysis of High Speed Pumps. RTO-EN-AVT-143, Paper 12. pp. 12-1 – 12-26, Neuilly-sur-Seine, France.

Visser, F. C., Dijkers, R. J. H., and op de Woerd, J. G. H. (2000). *Numerical Flow-Field Analysis and Design Optimization of a High-Energy First-Stage Centrifugal Pump*. In Computing and Visualization in Science, Vol. 3, No. 1-2, pp. 103-108.

White, F. M. (1974). *Viscous Fluid Flow*, 1st ed. New York: McGraw-Hill, Inc.